Saturated and Unsaturated Polymer Flows: Microphenomena and Modeling

F.D. DUNGAN AND A.M. SASTRY*

Department of Mechanical Engineering
2250 G.G. Brown Building
2350 Hayward Street
The University of Michigan
Ann Arbor, Michigan 48109-2125, USA

ABSTRACT: Fabrication of large composite parts via resin impregnation necessarily involves both saturated and unsaturated flow. While Darcy's law assumptions classically model only the saturated flow, the idea of a Darcy-type "permeability has been widely used to describe unsaturated flows as well. Differences between saturated and unsaturated resin flow through fibrous preforms have long been reported in the literature, however, and selection of permeability values for use in numerical simulation requires a clear understanding of the differences between these two flow types. Here, we present a new model for use in prediction of the ratios of these two permeabilities. Capillary effect and the fiber roughness are shown not to be dominant phenomena, as previously assumed by other workers. Instead, transverse flow into tows, which occurs after the fluid has permeated the intertow gaps, is found to produce significant differences in saturated and unsaturated flow velocities. Our model, which is based on Berman's flow in a channel with porous walls, additionally accounts for walls reaching saturation as the flow moves axially through the reinforcement phase, and is shown to be in agreement with earlier experimental data. We also present analyses and experimental results based on atomic force microscopy on fiber roughness, showing its effects on flow to be of less importance than the tow permeation process. The investigation on roughness shows convincingly that for practical materials, roughness is not a concern in flow retardation at any scale (fiber or tow).

KEY WORDS: permeability, saturated flow, unsaturated flow, intratow flow, intertow flow, capillarity, capillary flow, surface roughness.

INTRODUCTION

FABRICATION OF LARGE composite parts through resin infusion of fibrous preforms involves flow through unsaturated (dry) and saturated (pre-wetted) preform areas. Examples of large structural parts produced by resin transfer molding (RTM) include

---

*Author to whom correspondence should be addressed. E-mail: amsastry@umich.edu

body panels for the Dodge Viper, airplane engine fan-exit cases produced by Dow-UT, and propeller blades manufactured by Dowty such as the 6-bladed R391 propeller used on the Lockheed Martin C-130J aircraft. Defect-free production of these components requires modeling of the fluid penetration of the fabric in order to place ports and sequence injection times to prevent encapsulation of large dry areas, while simultaneously minimizing production times within the constraints of mold heating and resin cure [1]. However, flow through saturated preforms has been shown to be of different constitutive behavior than flow through unsaturated regions. Understanding the applicability of a saturation assumption is critical since full impregnation is far from instantaneous. The differences between the flow types can be characterized most easily for low-velocity flows by calculation or measurement of fabric permeability, through some application of Darcy's law [2].

Application of Darcy's law is widely used to model the flow of resin through reinforcements that are initially dry (unsaturated), though the relation is derived via assumption of steady-state flow through a statistically uniform saturated medium. Our previous findings [3,4] showed that microscale fluid modeling incorporating 3D fabric architecture satisfactorily predicted permeability, without time-consuming bench-scale experimentation typically associated with use of the Darcy approach. A particularly significant finding of that work was the importance of fabric layering and architecture, rather than capillarity or surface effects, in determining fabric permeability. We found good agreement between our experimental saturated permeabilities and the permeabilities obtained using our 3D fabric model to generate gap dimensions used for modeling flow. Recently, Chen and Chou [5,6] generated a similar 3D model for fabric in order to model compaction and thickness reduction for an undeformed balanced fabric in which the width of a representative cell is equal to the tow width (i.e., with no spacing between tows). In their model, the area of the tow cross-section is conserved, and the maximum thickness reduction is obtained by comparing the original thickness of a tow to the thickness of a rectangle with equivalent area. Our model [4], however, is more general, as it accounts for both intertow spacing and unbalanced warp and weft tow densities.

In this paper, we investigate the applicability of Darcy permeability to saturated versus unsaturated flows, building upon our previous experimental and numerical work. Unsaturated permeability, although not part of the steady-flow (Darcy, Poiseuille, etc.) framework, is taken to mean the fitted permeability in the case where the channel is not pre-wetted. Saturated permeability follows from the usual steady-flow assumption. We consider several key phenomena and material properties which have previously been identified in producing differences in saturated and unsaturated flow. We also develop a new model to capture the effect of saturation on permeability, through analysis of intratow and intertow flow using a porous wall model for penetration of fluid between porous walls (i.e. porous tows, in the present context). Finally, we suggest methodologies for both assessing the importance of saturation on fluid penetration into fabric preforms and validating our findings through comparison with our own bench-scale permeation experiments.

PREVIOUS WORK: SATURATED VERSUS UNSATURATED FLOW

The literature on use of the Darcy approach in modeling fluid penetration of resin preforms is quite extensive. Most of the published data collected here comparing saturated and unsaturated flows were generated for the purpose of evaluating permeability models

or values, rather than for the purpose of comparing the two types of flow. Consequently, few of these studies contain sufficient information to solely provide insight on flow differences. Nonetheless, we summarize the previous experimental findings in the next section, and reiterate a few conjectures on the causes of the differences. Next, we restate some of our own findings [3,4], motivating our theoretical investigation of flow differences.

Permeability Experimentation and Modeling

A summary of unsaturated versus saturated data generated by other workers is presented in Table 1. Ratios of saturated to unsaturated permeabilities greater than one [7–10], less than one [11,12] or varying slightly about one [13–16] have been reported.

Several authors [7,12,13] have invoked "channeling", i.e., fluid progressing in preferential paths in low volume fraction regions within the fiber bed, to account for flow differences in saturated and unsaturated conditions. This can occur at two scales, with intratow fiber rearrangement and full tow rearrangement. Within a tow, interfiber spacing, and thus intratow channeling, are minimized when fibers are regularly arranged [17]. Rearrangement of entire tows due to fluid flow can occur at high injection pressures, when inertial effects may induce fabric motion. Either type of flow-induced rearrangement can produce local areas of greater channel size, and thus enhance flow in the saturated condition.

The capillary effect has been put forward as another possible explanation for differences in saturated and unsaturated flows. Capillarity can also compound the effects of intertow and intratow rearrangement, altering permeability [11].

Air entrapped in the reinforcements by the flowing resin has also been mentioned as a possible cause. Williams et al. [7] speculated that entrapped air blocks pores in tows, resulting in higher Kozeny constants for dry beds.

Models have also been proposed to account for differences in saturated versus unsaturated flow due to the difference in apparent velocity caused by fluid penetration of the dry material. Parnas and Phelan [18] obtained numerical solutions for flow front movement by modeling dry fiber bundles as mass sinks which remove fluid from the flow as it advances through the mold. Pillai and Advani [19] used a sink term in the momentum equation to model unsaturated reinforcements as a two-phase porous medium. The resulting equations were solved numerically. These last two papers and similar efforts by these workers shared the characteristics of taking account of flow alteration in the channels by accounting for tow-level effects.

To summarize previous findings, flow channeling due to fiber or tow rearrangement, capillarity, air entrapment, and lower-speed fluid filling of unsaturated bundles have been suggested as possible explanations for differences in saturated and unsaturated fabric permeabilities. However, the literature spans several types of permeability experimentation, over a wide range of pressures and flow rates.

Motivation: Our Previous Findings

In our earlier, carefully controlled experiments with Knytex 24-5 × 4 plain-weave fabric and corn oil [3,4,20], we found ratios of saturated to unsaturated permeabilities to be greater than two on average, as shown in Table 2. A flow front from one of our saturated experiments is shown at several scales in Figure 1.

Table 1. Overview of literature reporting permeabilities for both saturated and unsaturated conditions.

Source	Types of Reinforcements	Type(s) of Fluid	Type(s) of Experiment	K_{sat}/K_{unsat}
Williams et al. (1974)	continuous E glass woven roving with silane size	oils, epoxy, glycerol	• flow through tube filled with fibers • applied pressure	1.19 for silicone oil, 1.13 for mineral oil, 1.27 for epoxy, 0.985 for glycerol (inversely proportional to the ratio of Kozeny constants)
Martin and Son (1986)	random mat, triaxial fabric, plain weave	corn syrup	• unidirectional flow • constant pressure drop	approximately 4
Foley and Gutowski (1991)	8 harness satin and plain weave carbon, 6 harness satin Kevlar	water, corn oil, mineral oils	• unidirectional flow • imposed pressure difference	between 0.247 and 1.34
Pollard (1992)	Woven and braided glass and graphite	oils	• unidirectional flow • constant flow rate	0.88–1.10 (ratio tended to be above 1 for most glass mats but was always below 1 for graphite mats)
Ahn et al. (1995)	glass plain weave fabric and glass chopped strand mat	corn oil	• unidirectional flow (sat) and radial flow (unsat) • constant inlet pressure	> 1
Parnas et al. (1995)	glass random mat and 3-D woven glass fabric	corn syrup diluted with water	• unidirectional flow (sat and unsat) and radial flow (unsat) • constant injection rate	varies over course of experiment. For woven fabric, initially > 1, then < 1, then goes to 1 after mold fills
Gebart and Lidström (1996)	highly anisotropic fabric and almost continuous strand mat	vinylester and vegetable oil	• unidirectional flow (sat and unsat) and radial flow (unsat) • imposed pressure difference	close to 1
Lekakou et al. (1996)	nearly isotropic plain weave glass fabric	silicone oil	• unidirectional flow and radial flow, sat and unsat for both (but unidirectional data not directly comparable (different Q's) • constant flow rate	> 1 (0.933 for $\varepsilon = 0.50$, 1.51 for $\varepsilon = 0.48$, 1.94 for $\varepsilon = 0.44$ (radial flow, $Q = 6.67 \times 10^{-7}$ m^3/s)
Hammond and Loos (1997)	glass plain weave and carbon 8-harness satin	water, corn oil, epoxy	• unidirectional flow • steady-state tests: constant flow rate, advancing front test: mostly constant pressure, some constant flow rate	close to 1
Lundström et al. (2000)	glass fabrics: 3-D weave, non-crimp stitched, and plain-weave	paraffin based oil, vinyl ester, and polyester	• unidirectional flow (sat and unsat) and radial flow (unsat) • constant driving pressure	slightly below 1 (saturated K's lower with radial method than with parallel flow method)

Table 2. Summary of experimental data of interest from our previous experiments [3,4].

Shear Angle		Unsaturated Conditions	Saturated Conditions	$\dfrac{K_{sat}}{K_{unsat}}$
0°	Average Experimental K_1 [$\times 10^{-10}\,\mathrm{m}^2$]	6.32	15.1	2.39
	Average Experimental K_2 [$\times 10^{-10}\,\mathrm{m}^2$]	5.45	12.6	2.31
15°	Average Experimental K_1 [$\times 10^{-10}\,\mathrm{m}^2$]	4.76	10.4	2.18
	Average Experimental K_2 [$\times 10^{-10}\,\mathrm{m}^2$]	3.36	7.17	2.13
30°	Average Experimental K_1 [$\times 10^{-10}\,\mathrm{m}^2$]	6.24	12.6	2.02
	Average Experimental K_2 [$\times 10^{-10}\,\mathrm{m}^2$]	3.61	6.38	1.77

(a)

(b)
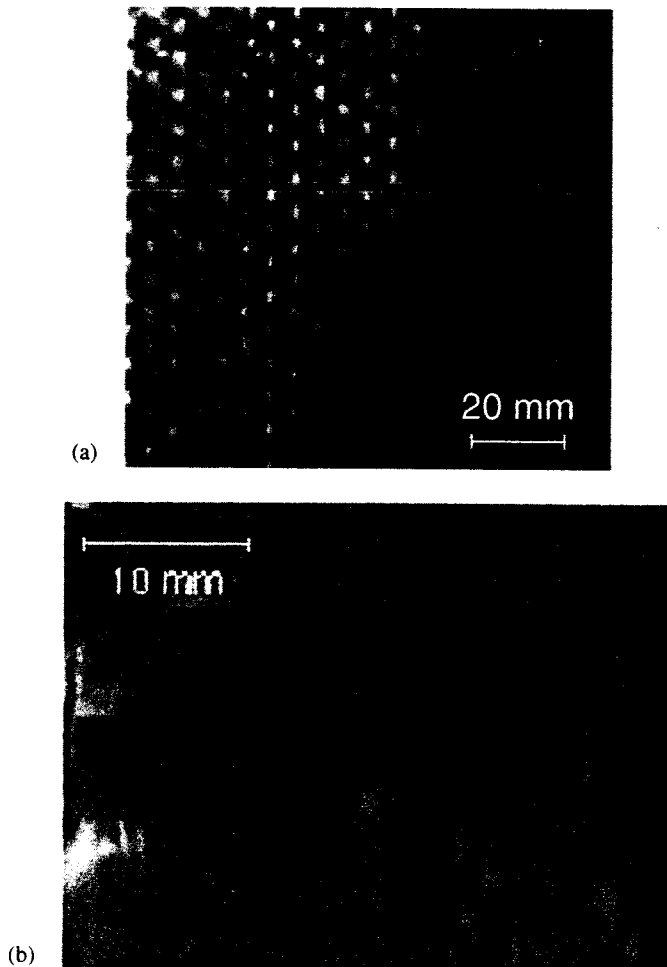
Figure 1. *Fluid penetrating Knytex 24-5 × 4 plain-weave fabric, shown at three scales: (a) fabric level, (b) tow level and (c) fiber (intratow) level.*

We observed no obvious flow-induced rearrangement of tows in our experiments (30–120 kPa injection pressures). Our general observation during all of the unsaturated experiments was that the flow first quickly penetrated the intertow gaps, and penetrated the tows a few seconds later. We explore this observation in greater detail below.
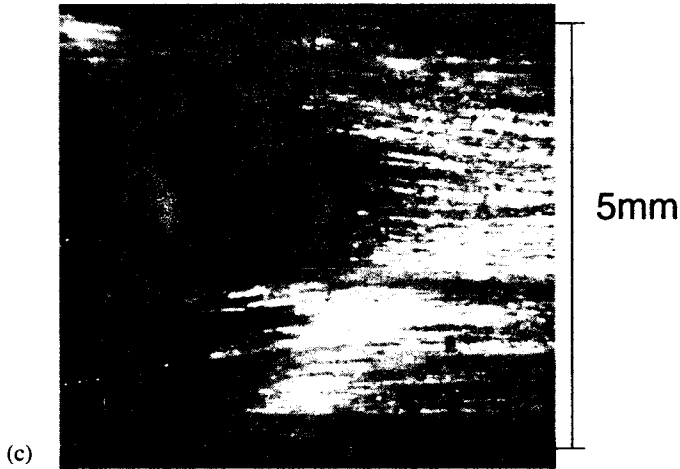
(c)

Figure 1. (Continued)

Capillarity at either the inter- or intratow scale can only play a significant role in flow in cases of very low injection pressures and flow rates. In our own studies, we determined from calculations and separate observations on tows that intertow flow clearly dominated intratow flow [3,4], so that capillarity could not have played a strong role in the observed differences in saturated and unsaturated permeabilities. Also, if capillarity had been the dominant phenomenon, permeabilities for unsaturated flow would have been higher than for saturated flow, which is the opposite of what we observed.

Based on our findings and suggestions in the literature, we investigated two possible explanations for the difference between unsaturated and saturated permeabilities:

1. *Surface roughness of fibers:* Saturation could mitigate the reduction in velocity due to such roughness, producing higher-velocity saturated flow versus unsaturated flow (i.e., ratios of saturated to unsaturated permeabilities greater than one). We investigated the effect of roughness using a model of channel flow with wall asperities.
2. *Longer penetration times in unsaturated flow due to required wetting of the tows:* Perpendicular flow into tows, which ends with tow saturation, slows down overall flow. Modeling of intratow penetration using a porous wall model was performed.

Based on a parametric study on roughness, we found little support for the first hypothesis. However, we found the second hypothesis to be consistent with experimental and theoretical findings; we describe our results below. We reserve our derivations and experimental findings on roughness for the Discussion section.

APPROACH: FLOW IN A CHANNEL WITH POROUS WALLS REACHING SATURATION

Here we derive relations for transverse fluid velocity, unsaturated length, and permeability ratio in a channel with porous walls with flow both parallel and transverse to the channel walls. "Unsaturated length" refers to a length along the channel in which fluid is flowing transversely into the channel walls.

The derivations follow from calculation of the velocity profile of a fluid through a channel with some length of porous and solid walls. The porous wall region is given a variable length behind the flow front; the solid wall region approximates full saturation.

Computation of Transverse Fluid Velocity

Flow is assumed to be driven into tows transversely by the capillary pressure; the pressure gradient driving the flow is in the channel direction. Capillary pressure is as per the Young–Laplace relation [e.g. 21],

$$P_c = \frac{4\sigma \cos(\psi)}{D_E} \qquad \circ \tag{1}$$

where σ is the surface tension, ψ the contact angle, and D_E the wetted diameter.

Lekakou and Bader [22] rewrote Ahn et al.'s [9] expression for the equivalent wetted diameter [23] as

$$D_E = \frac{8r_f}{F}\frac{\varepsilon}{(1-\varepsilon)} \tag{2}$$

where r_f is the radius of a filament and ε is the tow porosity. F is a form factor which takes a value of 4 for flow along a tow and 2 for flow transverse to a tow [22], so we write

$$P_c^T = \frac{\sigma \cos(\psi)(1-\varepsilon)}{r_f \varepsilon} \tag{3}$$

and

$$P_c^A = \frac{2\sigma \cos(\psi)}{r_f \varepsilon}(1-\varepsilon) \tag{4}$$

as the capillary pressures in the transverse (P_C^T) and axial (P_C^A) directions, respectively. Except for transverse capillary pressure (P_C^T), we hereafter denote transverse properties and functions with asterisks. The transverse fluid velocity can be calculated via Darcy's law as

$$u^* = \frac{-K^*}{\mu}\nabla P^*, \qquad \cdot \tag{5}$$

where

$$\nabla P^* = \frac{P_c^T}{h_{eq}}, \tag{6}$$

with h_{eq} taken as half the thickness of the equivalent volume of tows per representative cell, as shown in Figure 2, since fluid penetrated tows from both the top face and the bottom face. h_{eq} can be written as

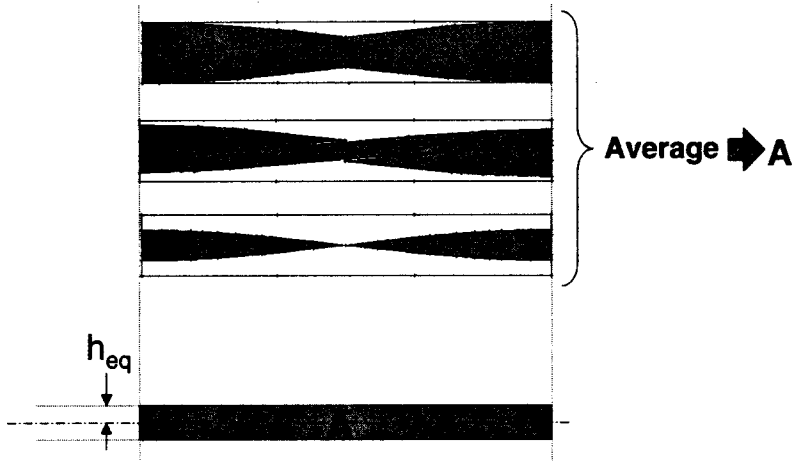$$h_{eq} = h(V_f^{\text{tow}}) \tag{7}$$

Figure 2. *Determination of channel wall width, based on volume of tows in a representative cell. The channel wall width is half the thickness (h_{eq}) of the average tow volume per representative cell.*

where $2h$ is the thickness of a fabric layer and V_f^{tow} the volume fraction of tows in a representative cell. K^*, the permeability of a tow in the transverse direction, is calculated via Gebart's approach [24] as

$$K^* = \frac{16}{9\pi\sqrt{6}} \left(\sqrt{\frac{V_{f\,max}}{V_f}} - 1 \right)^{5/2} r_f^2 \qquad (8)$$

where $V_{f max}$ is the maximum possible volume fraction of hexagonally-packed fibers, i.e., 0.907. The axial permeability [24] within a hexagonally packed tow is taken as

$$K_c^A = \frac{8 r_f^2}{53} \frac{(1 - V_f)}{V_f^2}. \qquad (9)$$

Computation of Permeability Ratio

Determining the velocity of the flow through a channel with porous walls was probably first undertaken by Berman [25], who considered the domain shown in Figure 3. This work has been widely referenced, with applications ranging from osmotic processes involved in water desalination [e.g. 26] to heat transfer in circular tubes and rectangular ducts [e.g. 27]. In the field of composites manufacturing, the model has been used to approximate flow between two porous cylindrical tows in an effort to model air entrapment [28]. In Berman's classical model, the width of the porous walls is infinite, which is certainly not a reasonable assumption in the present composites processing problem; we return to this point shortly.

Berman's solution [25] results in the velocity profile

$$u(x, \lambda) = \left[\bar{u}(0) - \frac{u^* x}{b} \right] \left[\frac{3}{2}(1 - \lambda^2) \right] \left[1 - \frac{Re}{420}(2 - 7\lambda^2 - 7\lambda^4) \right] \qquad (10)$$
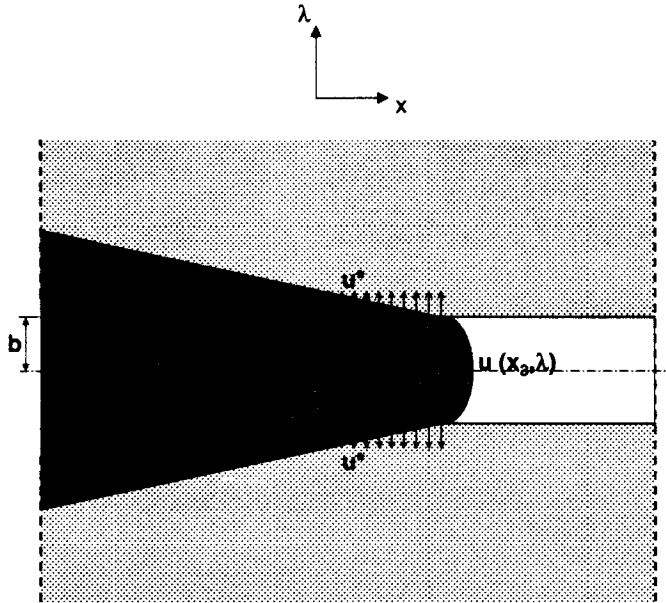
Figure 3. Schematic of flow in a channel with porous walls (Berman's model).

where u^* is the velocity in the transverse direction (into the walls), $\bar{u}_0$ the initial velocity in the x direction, $2b$ the thickness of the channel, λ the z coordinate normalized by b, and Re a Reynolds number defined by

$$\text{Re} \equiv \frac{u^* b \rho}{\mu}. \tag{11}$$

The pressure distribution in this model is given by

$$p(0,\lambda) - p(x,\lambda) = \frac{1}{2}\rho u_{\text{sat}}^2 \left[\left(\frac{24}{N_{\text{Re}}} - \frac{648}{35}\frac{R}{N_{\text{Re}}} \right) \left(1 - \frac{2R}{N_{\text{Re}}}\frac{x}{b} \right) \left(\frac{x}{b} \right) \right] \tag{12}$$

where N_{Re} is a Reynolds number for the flow entering the channel, defined as

$$N_{\text{Re}} = \frac{4bu_{\text{sat}}\rho}{\mu}. \tag{13}$$

Equation (12) reduces to the expression for plane Poiseuille flow if the transverse velocity into the walls (u^*) is zero. The transversely-averaged axial velocity changes linearly with x; the transverse velocity u^* (into the porous walls) is constant over the entire length of the walls.

For the case of present interest, clearly the porous "walls," i.e., the permeable fabric tows bounding the fabric channels, are finite, and have a width which can be determined from the tow geometry itself. Figure 4 illustrates the variable gap model in which flow in a particular direction is modeled using a trapezoidal channel [3,4] and the rectangular channel with equivalent permeability considered here. With this geometry, only the part of the wall that is within a distance L of the flow front, that is, the region between $x = x_s$ and $x = x_f$, is porous, as shown in Figure 5. In the region between $x = 0$ and $x = x_s$, the porous tows (walls) are completely saturated and u^* is zero, resulting in plane Poiseuille flow.
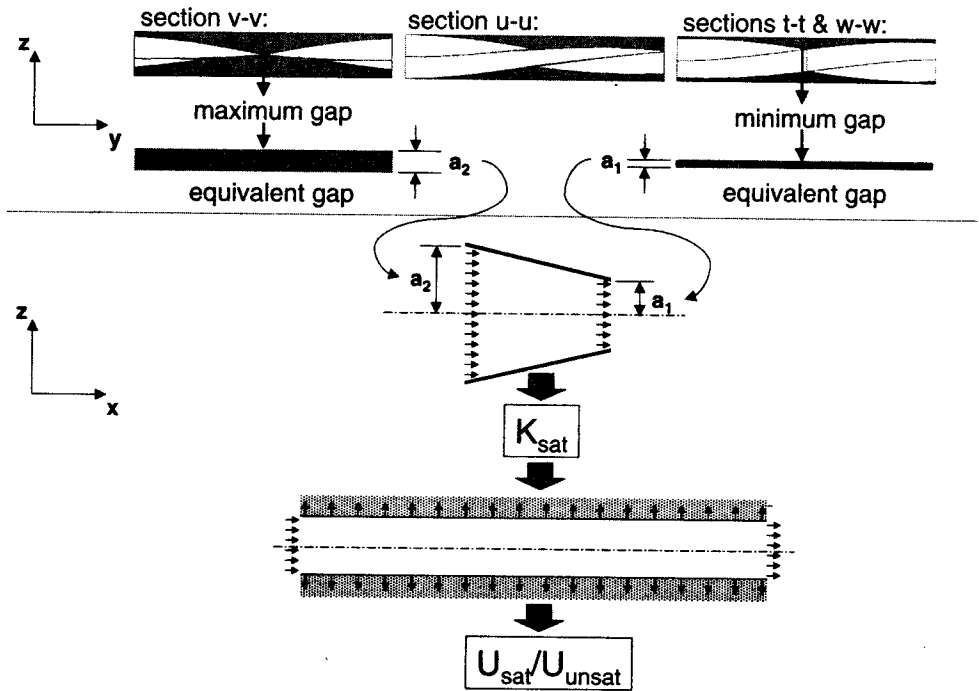
Figure 4. The variable gap model. 2-D cross-sections are shown in the middle, including section v-v, which contains the maximum gap, cross-section u-u, an example of a cross-section with intermediate gaps, and sections t-t and w-w, which combine to form the cross-section that contains the minimum gap. The variable-gap model (1-D) is shown at the bottom, with dimensions a_2 and a_1 obtained from the equivalent maximum and minimum gap thicknesses, respectively (adapted from [4]).
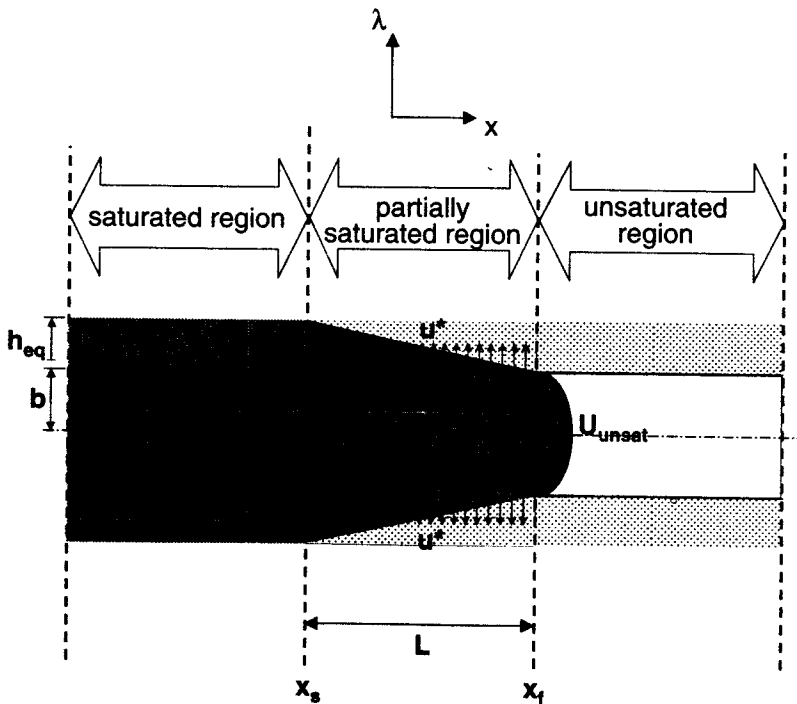

Figure 5. Schematic of flow in a channel with porous walls reaching saturation. There is a partially saturated region in the tow in which the fluid penetration is a linear function of axial length, as shown.

Using Berman's model [25], the average velocity over the region between $x = x_s$ and $x = x_f$ (averaged with respect to λ and x) can be written as

$$\frac{u_{\text{sat}} + u_{\text{unsat}}}{2} = \frac{\int_0^L \int_{-1}^1 u(x, \lambda) d\lambda dx}{L} = u_{\text{sat}} - \frac{u^* L}{2b}. \tag{14}$$

u_{sat} is the velocity at $x = x_s$ (the saturated velocity) and u_{unsat} is the velocity at $x = x_f$ (the unsaturated velocity).

The same expression can alternatively be obtained from a volumetric flow rate balance on the control volume limited by the channel walls between $x = x_s$ and $x = x_f$. Equating the volume flow rate of fluid into and out of the control volume and dividing through by the depth in the y dimension, Y, yields

$$u_{\text{sat}} b = u_{\text{unsat}} b + L u^* \tag{15}$$

which is equivalent to the average result (Equation (14)) from Berman's model [25].

The channel half-thickness, b, is taken as half the distance between two plates that yields an equivalent permeability to that obtained with the variable gap model using fabric geometry for the case of gaps between a layer of fabric and a flat surface [3,4], as shown in Figure 4. From Table 2 of [4], the equivalent permeability in the case of flow between infinite parallel plates (plane Poiseuille flow) is

$$K = \frac{b^2}{3} \tag{16}$$

and the equivalent permeability for the variable gap model [4] is

$$K = \frac{4}{3} \frac{a_1^2 a_2^2}{(a_1 + a_2)^2}, \tag{17}$$

where a_1 and a_2 are the end half-thicknesses of the trapezoidal channel. The width of the channel, b, is then calculated from Equations (16) and (17) as

$$b = \sqrt{4 \frac{a_1^2 a_2^2}{(a_1 + a_2)^2}}. \tag{18}$$

The actual volume of the walls must enter the analysis, since the velocity in the transverse direction must be zero when the walls are completely filled. The volume of the walls per unit depth (in the y direction) between $x = x_s$ and $x = x_f$ is

$$\frac{V^*}{Y} = 2L h_{eq} (1 - V_f)_{\text{corr}} \tag{19}$$

where

$$(1 - V_f)_{\text{corr}} = (1 - V_f) \left[-\sin \left(\left(\left(\frac{V_f}{V_{f,\,\text{max}}} \right)^n - 1 \right) \frac{\pi}{2} \right) \right] \tag{20}$$

is used instead of $(1 - V_f)$ since it vanishes as the volume fraction V_f goes to the maximum packing fraction $V_{f,\text{max}}$. A value of $n = 20$ is used here, based on a sensitivity analysis on this parameter. In using a high value of n, the effect of the correction is essentially nonexistant away from the maximum volume fraction. A higher value of n would offer no real advantage.

The volume flow rate of fluid into the walls per unit depth between $x = x_s$ and $x = x_f$ is

$$\frac{Q^*}{Y} = (u^*)2L, \tag{21}$$

The time required for the fluid to completely fill the volume of the porous walls between $x = x_s$ and $x = x_f$ is calculated from Equations (19) and (21) as

$$t_L = \frac{h_{eq}(1 - V_f)_{\text{corr}}}{u^*} \tag{22}$$

The fluid in the channel covers the axial distance L in time t_L (Figure 5). We also write t_L as

$$t_L = \frac{L}{0.5(u_{\text{sat}} + u_{\text{unsat}})} \tag{23}$$

and equate the two relations (Equations (22) and (23)) to solve for L as

$$L = \frac{h_{eq}(1 - V_f)_{\text{corr}}(u_{\text{unsat}} + u_{\text{sat}})}{2u^*}. \tag{24}$$

Substituting into Equation (14), we can express the ratio of saturated to unsaturated velocities as

$$\frac{u_{\text{sat}}}{u_{\text{unsat}}} = \frac{2b + h_{eq}(1 - V_f)_{\text{corr}}}{2b - h_{eq}(1 - V_f)_{\text{corr}}}. \tag{25}$$

Applying Darcy's law to the region between $x = 0$ and $x = x_f$, we find

$$u_{\text{unsat}} = \frac{K_{\text{unsat}}}{\mu} \frac{P_{inj} - P|_{x=x_f}}{\Delta L}. \tag{26}$$

Similarly, we apply Darcy's law to the region between $x = 0$ and $x = x_s$, yielding

$$u_{\text{sat}} = \frac{K_{\text{sat}}}{\mu} \frac{P_{inj} - P|_{x=x_s}}{\Delta L - L}. \tag{27}$$

The pressure drop between $x = x_s$ and $x = x_f$ is obtained with Berman's model (Equation (12)) and the pressure at $x = x_f$ is known (usually atmospheric); thus, the pressure at $x = x_s$ is known also. Using this relation and combining with Equations (26) and (27),

the ratio of permeabilities can be expressed as

$$\frac{K_{sat}}{K_{unsat}} = \frac{u_{sat}}{u_{unsat}} \frac{\Delta L - L}{\Delta L} \frac{P_{inj} - P|_{x=x_f}}{P_{inj} - P|_{x=x_s}}. \tag{28}$$

In analysis of our data, we used the average radius of the flow front towards the end of our experiments as ΔL [3]. In the limit as ΔL goes to infinity, the ratio of permeabilities go to values about 50% higher than the ones obtained for the ΔL based on the experimental mold geometry. Properties [4] and intermediate results for the case of interest here are shown in Table 3. Results for ratios of calculated saturated to unsaturated quantities are given for velocity and permeability in Table 4 for both principal directions. These results are based entirely on fabric geometry, materials properties and calculated parameters, and involve no fitting parameters.

Table 3. Measured, fitted and calculated quantities used in model of channel with porous walls reaching saturation.

σ, surface tension of corn oil	30.1×10^{-3} N/m
ψ, contact angle of corn oil on glass	$20.1°$
r_f, radius of glass filament	8.6×10^{-6} m
F, shape factor	2
V_f, intra-tow fiber volume fraction	0.786
b, half height of flow channel for $\theta = 0°$	5.21×10^{-5} m
b, half height of flow channel for $\theta = 15°$	7.79×10^{-5} m
b, half height of flow channel for $\theta = 30°$	7.71×10^{-5} m
ρ, density of corn oil	983 kg/m^3
μ, viscosity of corn oil	0.040 Pa s
D_E, equivalent wetted diameter	9.36×10^{-6} m
P^c, transverse capillary pressure	12,100 N/m^2
ΔL^*, 1/2 tow thickness of Knytex 24-5 × 4 fabric	1.84×10^{-4} m
K^*, transverse permeability of tow	2.56×10^{-14} m^2
V^*, transverse fluid velocity	4.20×10^{-5} m/s
$t_{1/2tow}$, time to permeate half the tow thickness	4.38 s
ΔL, average distance between injection hole and edge of flow front at end of experiments	0.12 m

Table 4. Calculated ratios of saturated to unsaturated velocities and permeabilities for Knytex 24-5 × 4 with shear angles 0, 15, and 30°. The distance between plates used here results in the same channel permeability as the variable gap model for the indicated shear angles. All data in the table were obtained from fabric geometry and calculations. No fitting parameters were used.

Shear Angle	Equivalent b (VGM) [m]	Calculated K_{sat}/K_{unsat}
0°	5.21×10^{-5}	2.77
15°	7.79×10^{-5}	2.18
30°	7.71×10^{-5}	2.19

DISCUSSION

We divide our comments into those on applicability of the finite permeable wall model and those on the effects of fiber roughness and the slip boundary condition.

Applicability of the Finite Permeable Wall Model

In developing our model, we neglected the effect of axial capillary action on fluid motion. To assure that the effect of this axial capillarity was small, we calculated the ratio of t_L, the time it takes to saturate the channel walls, to t_c^A, the time it takes the fluid to travel an axial distance L within the tows (walls) under the influence of the axial capillary pressure, P_c^A. The axial time t_c^A can be expressed as the ratio of the distance traveled, L, to the Darcian velocity of the fluid in the tow, or

$$t_c^A = \frac{L^2 \mu}{K_c^A P_c^A} \tag{29}$$

Combining Equations (22), (23), and (29), we write

$$\frac{t_L}{t_c^A} = \frac{4u^* K_c^A P_c^A}{h_{eq}(1 - V_f)_{\text{corr}} \mu [u_{\text{sat}}(1 + (u_{\text{unsat}}/u_{\text{sat}}))]^2} \tag{30}$$

For our case, using quantities in Table 3, the above ratio for the average injection pressure and average b was found to be below 1.5×10^{-4}, that is, 1/6700, for the three shear angles.

We also neglected the effect of axial pressure on transverse tow penetration. Incorporation of this effect would probably require a tow-level model which accounts for the actual flow front/tow boundary in a fabric, which is a level of detail not used here. It is questionable whether such a study would produce practical guidance for manufacturers.

A possible source of error in our model is the fact that the surface area in contact with the fluid in the actual channel is higher than in the case of flat plates, as shown in Figure 6a. Another source of error from the channel being flat plates rather than actual tows is that the fluid would advance through the entire thickness of a tow near its narrower edges, which would then allow the fluid to penetrate the remaining, thicker section transversely as well as axially (Figure 6b). Given the agreement in the data and the investigation of other flow phenomena that follows, we assess these effects to be rather small.

Fiber Roughness and the Slip Boundary Condition

We investigated flow in rough pipes and flow over rough surfaces as models for the type of flow retardation we might encounter in the composite process, due to surface roughness of the filaments. Flow in rough pipes has been studied extensively. Early work by Nikuradse [29] resulted in the formulation of laws describing turbulent flow in rough
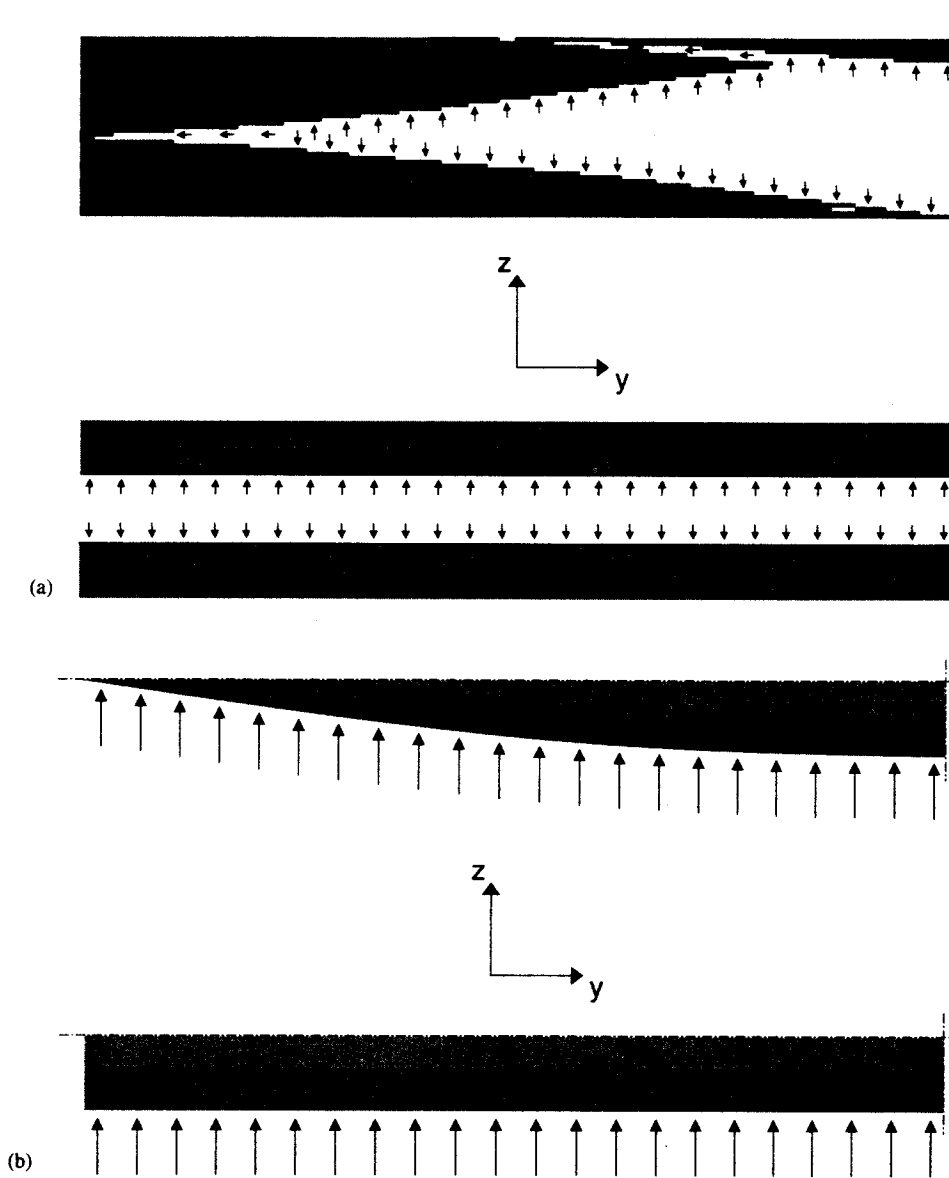
Figure 6. *Actual channel geometry versus model: cross-sections transverse to tow direction showing fluid penetration into channel walls. (a) Typical gap shape versus rectangular channel. (b) Actual versus strictly one-dimensional impregnation of tow. Schematics are symmetric about the "dash-dot-dash" lines.*

pipes. Subbotin et al. [30] conducted an experimental study of pressure drop and velocity fields in rough pipes, for laminar and turbulent flows. Lamont's work [31] includes recommendations for roughness factors for a variety of pipes.

Studies on flow over rough surfaces include the work of Schlichting [32], who conducted an experimental study of flow in a rectangular channel with varying roughness. Knight and Macdonald investigated behavior in large channels [33]. Mickaily et al. [34] studied the motion of steel bobs with various surface roughnesses in a viscous liquid. Higdon [35] and Levchenko and Ukhov [36] performed numerical work on flow over rough surfaces. Elrod [37] derived general relations for the behavior of thin lubricating films in the presence of roughness.

Many authors have used a slip boundary condition to account for the roughness of the surface over which fluid is flowing, based on the boundary condition described by Navier (see historical overview in Goldstein [38]). Beavers and Joseph [39] studied flow over a porous block experimentally, and developed a theory for flow dynamics based on replacement of the boundary layer effect with a slip velocity. Building on their work, Richardson [40] presented a model and analysis for experiments performed by Taylor [41] for flow in a small gap above a porous medium made of parallel plates. In these cases [39,40,41], flow at the solid boundary is enhanced due to fluid velocity in the porous medium, unlike flow over a rough surface, which is impeded by the roughness at the boundary.

Sarkar and Prosperetti [42] represented the effect of roughness on flow far from the boundary by replacing the no-slip condition on the exact boundary by a partial slip condition on a smooth surface. They looked at what they termed "bumpy surfaces," which have finite surface slope irrespective of the size of the irregularities. Miksis and Davis [43], Tuck and Kouzoubov [44], and Hocking [45], among others, did similar work for what Sarkar and Prosperetti [42] termed "wavy surfaces," in which both the scale of surface irregularities and their slopes are small. Jansons [46] looked at bumpy surfaces and showed a perfect slip boundary to be consistent with macroscopic observations of real surfaces.

In order to determine whether the roughness of the fibers was a significant impediment to the flow, a model system of steady flow between two infinite plates separated by a distance $2b$ was investigated. The main steps of the derivation follow. All parameters are constant with respect to the y direction.

Starting with the x component of the Navier–Stokes equations

$$\frac{\partial P}{\partial x} = \mu\left(\frac{\partial^2 u}{\partial x^2} + \frac{\partial^2 u}{\partial z^2}\right) \tag{31}$$

and the continuity equation

$$\frac{\partial u}{\partial x} + \frac{\partial v}{\partial y} + \frac{\partial w}{\partial z} = 0, \tag{32}$$

we take $v = w = 0$, since fluid motion is in the x direction only. The continuity equation reduces to

$$\frac{\partial u}{\partial x} = 0 \tag{33}$$

and the x component of the Navier–Stokes equations becomes

$$\frac{\partial P}{\partial x} = \mu\frac{\partial^2 u}{\partial z^2}. \tag{34}$$

Treating $\partial P/\partial x$ as a constant, a solution to the above equation has the form

$$u = \frac{1}{2\mu}\frac{\partial P}{\partial x}z^2 + c_1 z + c_2. \tag{35}$$

Imposing slip boundary conditions at the surface of both plates [45,46], we obtain

$$u(b) = -\langle R\rangle \frac{\partial u}{\partial z} \tag{36}$$

$$u(-b) = -\langle R\rangle \frac{\partial u}{\partial z} \tag{37}$$

where $\langle R\rangle$ is the RMS roughness of the plates, defined in Figure 7.
    Substitution of (36) and (37) into (35) yields

$$c_1 = -\frac{\langle R\rangle}{\mu} \frac{\partial P}{\partial x} \tag{38}$$

and

$$c_2 = \frac{1}{\mu}\frac{\partial P}{\partial x}\left(\langle R\rangle^2 - \frac{b^2}{2}\right). \tag{39}$$

The velocity can now be expressed as

$$u = \frac{1}{\mu}\frac{\partial P}{\partial x}\left(\frac{z^2}{2} - \langle R\rangle z + \langle R\rangle^2 - \frac{b^2}{2}\right) \tag{40}$$

The roughness of glass filaments from Knytex 24-5 × 4 was obtained using an atomic force microscope (NanoScope IIIa from Digital Instruments [47]), using both contact and tapping modes. RMS roughness values were obtained by averaging results for several sample surfaces of a given size. Patch sizes investigated ranged between 1 × 1 μm and 10 × 10 μm (based on the geometry of the cantilever tip, the absolute maximum square patch scannable for a fiber with a diameter of 17.2 μ is 13.4 × 13.4 μm.) The velocity profile
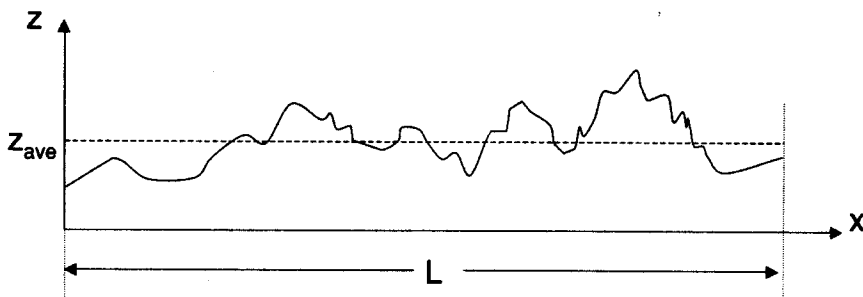
$$<R> = \sqrt{\frac{1}{N}\sum_{i=1}^{N}\left(z_i - z_{ave}\right)^2}$$

Figure 7. *Definition of RMS roughness. N is the number of points at which z is measured in the interval of length L, z_{ave} is the average z value over the interval.*

from Equation (40) was obtained based on a ratio of $b/\langle R \rangle$, or half the distance between the parallel plates to the average RMS roughness. Even when the largest measured value of roughness is used, the ratio $b/\langle R \rangle$ is over 100, resulting in no significant roughness effect on the fluid velocity, as shown in Figure 8.

Thus, despite the slowing of flow due to boundary roughness, the average roughness would have to be at least one order of magnitude larger than the largest roughness observed in order for this phenomenon to meaningfully affect the flows studied here.

CONCLUSIONS AND FUTURE WORK

A one-dimensional model was derived for flow between parallel plates separated by a distance yielding an equivalent permeability to that obtained with the variable gap model for the fabric layer-flat surface case [4]. In the present work, the planar walls were modeled as porous over a particular distance behind the flow front (determined by the time it takes fluid to go through the thickness of the equivalent volume of tows in a representative cell). This finite permeable wall model provides a good approximation of the experimental results recorded (Tables 2 and 4).

Several authors have found unsaturated flow to be faster than saturated flow in similar experiments. We postulate several reasons for this finding. First, the experimental method
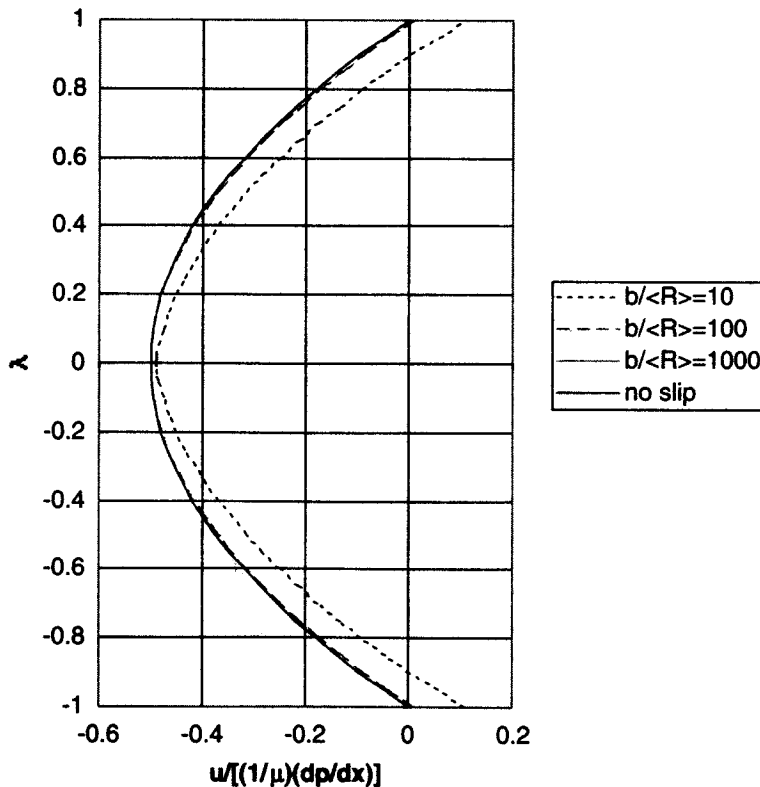

Figure 8. Axial velocity profiles for different values of $b/\langle R \rangle$ ratio.

used to obtain permeabilities may have affected results. Besides our own, the work of Lekakou et al. [10] was the only case we encountered wherein the radial flow technique was used to obtain both unsaturated and saturated permeabilities. They found K_{sat} to be greater than K_{unsat}. Second, differences in experimental parameters, techniques, materials, etc., could explain the wide variety of K_{sat}/K_{unsat} ratios reported in the literature. For example, a very low injection pressure could render capillary action significant in comparison with the intertow flow, and therefore, decrease the K_{sat}/K_{unsat} ratio substantially.

We observed in our laboratory that results were the same when permeability was measured at different stages of the injection, provided it was not at the very beginning of the injection. We also observed that a drop of fluid deposited at the center of one side of a single tow took an average of 2–3 s to reach the other side (this involved only the center of the tow, care was taken to avoid getting the thin tow edges wet). The results obtained with the model presented above are consistent with these observations. As shown in [3] and [4], the effects of nesting on permeability are even greater than those of saturation; however, the mechanism of nesting and its effects are understood and were described in [3] and [4].

Our findings suggest that ratios of two for ratios of saturated to unsaturated permeabilities are entirely plausible in light of the modeling and experiments here. This has important consequences for design of injection processes for large parts. In using numerical flow models involving local permeability descriptions, care must be taken to alter permeabilities in the numerical simulation when saturation is likely to have been achieved in a portion of a part, since permeability can increase by a factor of two after saturation. Accurate flow tracking and predictions of dry area entrapment depend on accurate permeation modeling. Thus, we suggest that closed form analysis such as that performed here be used to alter permeability during a numerical simulation of the permeation process, as appropriate, with use of proper material and geometrical properties.

We found that intra- and intertow density and filament-liquid interface characteristics, rather than the surface roughnesses of individual filaments, are much more important in material selection and design of resin impregnation processes. We also reiterate our earlier finding of the critical effect of fabric geometry on permeation, particularly the transverse stacking of layers. The finding here that the permeation process in the tows takes place at a markedly longer timescale than that in the intertow regions strongly reinforces that finding.

Future work on different fabric geometries is merited, particularly works in which transverse stacking geometries are thoroughly investigated, since both saturated and unsaturated permeabilities can be determined from modeling with no fitting parameters. Also, we find that future work on prediction of fabric permeabilities without reliance on bench-scale experiments is generally merited.

NOMENCLATURE

a_i = thickness of equivalent channel at either end ($i = 1, 2$)
b = half distance between plates
D_E = equivalent wetted diameter
F = form factor
h = tow thickness
h_{eq} = channel wall thickness, equal to fabric layer half-thickness times volume fraction of tows in representative cell

K = permeability

K_1 = first principal permeability (larger principal permeability)

K_2 = second principal permeability

K^* = transverse permeability of a tow

K_c^A = axial permeability of a tow

L = unsaturated length

N_{Re} = Reynold's number for flow entering channel

p^1 = dynamic pressure gradient

P_c^A = capillary pressure in the axial direction

P_c^* = capillary pressure in the transverse direction

ΔP = pressure difference

∇P^* = transverse pressure gradient

Q = fluid flow rate in tube

Q^* = volume flow rate of fluid into the walls between $x = x_s$ and $x = x_f$

R = pipe diameter

$\langle R \rangle$ = average roughness

r_f = filament radius

Re = Reynolds number

t_c^A = time for fluid to travel axial distance L within tow , driven by P_c^A

t_L = time to saturate the channel walls

u_0 = initial velocity

u_{unsat} = unsaturated fluid velocity, at $x = x_{ff\text{-}Lunsat}$

u_{sat} = saturated fluid velocity, at $x = x_{ff}$

u^* = transverse fluid velocity

V^* = volume of the walls (tows) between $x = x_s$ and $x = x_f$

V_f = fiber volume fraction

V_{fmax} = maximum fiber volume fraction, hexagonal packing

V_f^{tow} = volume fraction of tows in a representative cell

w = width of a tow

x_f = coordinate of flow front location

x_s = coordinate equal to x_f-L

Y = channel depth in the y direction

ε = tow porosity

μ = fluid viscosity

ρ = fluid density

σ = surface tension

ψ = contact angle

Superscripts

T = transverse

A = axial

Abbreviations

sat = saturated flow conditions

unsat = unsaturated flow conditions

VGM = variable gap model [3,4]

ACKNOWLEDGMENTS

REFERENCES

1. Sastry, A.M. (2000). Impregnation and consolidation phenomena. In: Zweben, C. and Kelly, A. (eds.), *Comprehensive Composite Materials*. Vol. II, Chapter 17. Elsevier.

2. Darcy, H. (1856). *Les fontaines publiques de la ville de Dijon*. Paris: Dalmont.

3. Dungan, F.D., Senoguz, M.T., Sastry, A.M. and Faillaci, D.A. (2001). Simulations and experiments on low-pressure permeation of fabrics: Part I – 3D modeling of unbalanced fabric. *Journal of Composite Materials*, 35(14): 1250–1284.

4. Senoguz, M.T., Dungan, F.D., Sastry, A.M. and Klamo, J.T. (2001). Simulations and experiments on low-pressure permeation of fabrics: Part II – the variable gap model and prediction of permeability. *Journal of Composite Materials*, 35(14): 1285–1327.

5. Chen, B. and Chou, T.-W. (1999). Compaction of woven-fabric preforms in liquid composite molding processes: single-layer deformation. *Composites Science and Technology*, 58: 1519–1526.

6. Chen, B. and Chou, T.-W. (2000). Compaction of woven-fabric preforms: nesting and multi-layer deformation. *Composites Science and Technology*, 60: 2223–2231.

7. Williams, J.G., Morris, C.E.M. and Ennis, B.C. (1974). Liquid flow through aligned fiber beds. *Polymer Engineering and Science*, 14(6): 413–419.

8. Martin, G.Q. and Son, J.S. (1986). Fluid mechanics of mold filling for fiber reinforced plastics. In: *Proceedings of the 2nd Conference on Advanced Composites*. Dearborn, MI. pp. 149–157.

9. Ahn, S.H., Lee, W.I. and Springer, G.S. (1995). Measurement of the three-dimensional permeability of fiber preforms using embedded fiber optic sensors. *Journal of Composite Materials*, 29(6): 715–733.

10. Lekakou, C., Johari, M.A.K., Norman, D. and Bader, M.G. (1996). Measurement techniques and effects on in-plane permeability of woven cloths in resin transfer moulding. *Composites: Part A*, 27A: 401–408.

11. Lundström, T.S., Stenberg, R., Bergström, R., Partanen, H. and Birkeland, P.A. (2000). In-plane permeability measurements: a nordic round-robin study. *Composites: Part A*, 31: 29–43.

12. Foley, M.F. and Gutowski, T. (1991). The effect of process variables on permeability in the flexible resin transfer molding (FRTM) process. 23rd International SAMPE Technical Conference.

13. Pollard, M. (1992). Permeabilities of fiber mats used in resin transfer molding. 24th International SAMPE Technical Conference. pp. T408–T420.

14. Parnas, R.S., Howard, J.G., Luce, T.L. and Advani, S.G. (1995). Permeability characterization. Part 1: a proposed standard reference fabric for permeability. *Polymer Composites*, 16(6): 429–445.

15. Gebart, B.R. and Lidström, P. (1996). Measurement of in-plane permeability of anisotropic fiber reinforcements. *Polymer Composites*, 17(1): 43–51.

16. Hammond, V.H. and Loos, A.C. (1997). The effects of fluid type and viscosity on the steady-state and advancing front permeability behavior of textile performs. *Journal of Reinforced Plastics and Composites*, 16(1): 50–72.

17. Gutowski, T.G., Cai, Z., Bauer, S., Boucher, D., Kingery, J. and Wineman, S. (1987). Consolidation experiments for laminate composites. *Journal of Composite Materials*, **21**: ·650–669.

18. Parnas, R.S. and Phelan, Jr., F.R. (1991). The effect of heterogeneous porous media on mold filling in resin transfer molding. *SAMPE Quarterly*, **22**(2): 53–60.

19. Pillai, K.M. and Advani, S.G. (1998). A model for unsaturated flow in woven fiber preforms during mold filling in resin transfer molding. *Journal of Composite Materials*, **21**(19): 1753–1783.

20. Dungan, F.D., Senoguz, M.T., Sastry, A.M. and Faillaci, D.A. (1999). On the use of Darcy permeability in sheared fabrics. *Journal of Reinforced Plastics and Composites*, **18**(5): 472–484.

21. Scheidegger, A.E. (1974). *The Physics of Flow through Porous Media*. Toronto: University of Toronto Press.

22. Lekakou, C. and Bader, M.G. (1998). Mathematical modelling of macro- and micro-infiltration in resin transfer moulding (RTM). *Composites Part A*, **29**A: 29–37.

23. Ahn, K.J., Seferis, J.C. and Berg, J.C. (1991). Simultaneous measurements of permeability and capillary pressure of thermosetting matrices in woven fabric reinforcements. *Polymer Composites*, **12**(3): 146–152.

24. Gebart, B.R. (1992). Permeability of unidirectional reinforcements for RTM. *Journal of Composite Materials*, **26**(8): 1100–1133.

25. Berman, A.S. (1953). Laminar flow in channels with porous walls. *Journal of Applied Physics*, **24**(9): 1232–1235.

26. Sherwood, T.K., Brian, P.L.T., Fisher, R.E. and Dresner, L. (1965). Salt concentration at phase boundaries in desalination by reverse osmosis. *Industrial and Engineering Chemistry Fundamentals*, **4**(2): 113–118.

27. Raithby, G. (1971). Laminar heat transfer in the thermal entrance region of circular tubes and two-dimensional rectangular ducts with wall suction and injection. *International Journal of Heat and Mass Transfer*, **14**: 223–243. Erratum, pp. 1881.

28. Chen, Y.-T. Macosko, C.W. and Davis, H.T. (1995). Wetting of fiber mats for composites manufacturing: II. air entrapment model. *AIChE Journal*, **41**(10): 2274–2280.

29. Nikuradse, J. (1933). Laws on flow in rough pipes. NACA technical memorandum 1292. Translation of *Stroemungsgesetze in rauhen Rohren*.

30. Subbotin, V.I., Ibragimov, M.K.H., Taranov, G.S. and Gusakov, V.I. (1978). Flow in pipes with regular, artificially-produced wall roughness. *Fluid Mechanics – Soviet Research*, **7**(1): 80–86.

31. Lamont, P.A. (1981). Common pipe flow formulas compared with the theory of roughness. *Journal – American Water Works Association*, **73**(5): 274–280.

32. Schlichting, H. (1936). Experimental investigation of the problem of surface roughness. NACA TM-823. Translation of *Experimentalle Untersuchungen zum Rauhigkeitsproblem*. *Ingenieur-Archiv*, **7**(1): 1–34.

33. Knight, D.W. and Macdonald, J.A. (1979). Open channel flow with varying bed roughness. *Journal of the Hydraulics Division – ASCE*, **105**(9): 1167–1183.

34. Mickaily, E.S., Middleman, S. and Allen, M. (1992). Viscous flow over periodic surfaces. *Chemical Engineering Communications*, **117**: 401–414.

35. Higdon, J.J.L. (1985). Stokes flow in arbitrary two-dimensional domains: shear flow over ridges and cavities. *Journal of Fluid Mechanics*, **159**: 195–226.

36. Levchenko, Y.D. and Ukhov, V.A. (1990). Hydrodynamics of channels with regular roughness at small Reynolds-numbers. *Soviet Atomic Energy*, **68**(6): 502–509.

37. Elrod, H.G. (1979). General theory of laminar lubrication with Reynolds roughness. *Journal of Lubrication Technology, Transactions of the ASME*, **101**(1): 8–14.

38. Goldstein, S. (ed.) (1938). *Modern Developments in Fluid Dynamics*. Oxford: Clarendon Press.

39. Beavers, G.S. and Joseph, D.D. (1967). Boundary conditions at a naturally permeable wall. *Journal of Fluid Mechanics*, **30**: 197–207.

40. Richardson, S. (1971). A model for the boundary condition of a porous material. Part 2. *Journal of Fluid Mechanics*, **49**: 327–336.

41. Taylor, G.I. (1971). A model for the boundary condition of a porous material. Part 1. *Journal of Fluid Mechanics*, **49**: 319–326.

42. Sarkar, K. and Prosperetti, A. (1996). Effective boundary conditions for Stokes flow over a rough surface. *Journal of Fluid Mechanics*, **316**: 223–240.

43. Miksis, M.J. and Davis, S.H. (1994). Slip over rough and coated surfaces. *Journal of Fluid Mechanics*, **273**: 125–139.

44. Tuck, E.O. and Kouzoubov, A. (1995). A laminar roughness boundary condition. *Journal of Fluid Mechanics*, **300**: 59–70.

45. Hocking, L.M. (1976). A moving fluid on a rough surface. *Journal of Fluid Mechanics*, **76**: 801–817.

46. Jansons, K.M. (1988). Determination of the macroscopic (partial) slip boundary condition for a viscous flow over a randomly rough surface with a perfect skip microscopic boundary condition. *Physics of Fluids*, **31**(1): 15–17.

47. Digital Instruments, Incorporated, 112 Robin Hill Road, Santa Barbara, CA 93117.